A Chip-Scale, Low Cost PVD System

Lawrence K. Barrett, Richard Lally, Nicholas E. Fuhr, Alexander Stange, and David J. Bishop, *Member, IEEE*

Abstract—Standard physical vapor deposition systems are large, expensive, and slow. As part of an on-going effort to build a fab-on-a-chip, we have developed a chip-scale, low cost, fast physical vapor deposition system consisting of two MEMS devices: a chip-scale thermal evaporator and a mass sensor that serves as a film thickness monitor. Here, we demonstrate the functionality of both devices by depositing Pb thin-films. The thermal evaporator was made by fabless manufacturing using the SOIMUMPs processs (MEMSCAP, inc). It turns on in $1.46\,\mathrm{s}$ and reaches deposition rates as high as $7.2\,\mathrm{\AA\,s^{-1}}$ with $\sim 1\,\mathrm{mm}$ separation from the target. The mass sensor is a re-purposed quartz oscillator (JTX210) that is commercially available for less than one dollar. Its resolution was measured to be $2.65\,\mathrm{fg}$ or 7.79E-5 monolayers of Pb.

Index Terms—Physical Vapor Deposition (PVD), Evaporation, Fab-on-a-chip, MEMS, Mass sensor, Quartz Oscillator, Film Thickness Monitor, Phased Locked Loop

I. INTRODUCTION

PHYSICAL vapor deposition (PVD) is a widely used method for thin film growth in which material is vaporized from a source, transported as a vapor, and condensed onto a target [1]–[3]. It is used in a wide range of applications including coatings [4], diffusion barriers [5], micro/nanoelectronics [6], [7], magnetic films for data storage [8]–[10], synthesis of 2D materials [11], [12], synthesis of quench condensed superconductors [13]–[16], and synthesis of nano/micro patterned metal structures [17]–[20]. Generally, these systems are large, expensive, and slow to start and stop deposition. They make up for it by being able to process many devices at a time.

As part of an on-going effort to build a fab-on-a-chip (FoC) [21], we have developed a chip-scale, rapid, and inexpensive PVD system that has advantages for certain applications. The system is composed of two microelectromechanical systems (MEMS) based devices: a chip-scale thermal evaporator and a mass sensor made from a commercial quartz oscillator. These two devices combine into a PVD system that can start/stop deposition in less than $1.5\,\mathrm{s}$, and has a volume of less than $1\,\mathrm{cm^3}$ (not including a necessary vacuum system). It also consumes less than $200\,\mathrm{mW}$ of power inside the vacuum chamber which is an important measure because it puts an upper limit on the amount of heat generated within the system.

L. K. Barrett, R. Lally, N. E. Fuhr, and A. Stange are with the Division of Materials Science, Boston University, Boston, MA 02215 USA (e-mail: blawrenc@bu.edu; rlally@bu.edu; fuhrnick@bu.edu; stange@bu.edu).

D. J. Bishop is with the Division of Materials Science, Electrical and Computer Engineering Department, Physics Department, Department of Mechanical Engineering, Department of Biomedical Engineering, Boston University, Boston, MA 02215 USA (e-mail: djb1@bu.edu).

Manuscript received ???

Additionally the system is low-cost. The thermal evaporator is made by fabless manufacturing [22], [23] using a multi-user commercial foundry process, and the mass sensor is a commercially available device costing less than one dollar.

These characteristics give the chip-scale system advantages over over traditional PVD systems in certain applications. For example, because of the low power consumption, the system is safer, and produces less heat. The decreased heat production allows the system to be used with heat-sensitive targets such as certain organic films and heat-sensitive environments such as a cryostat. The low power output also decreases thermal drift without the need for active temperature controls which is particularly important in dynamic stencil lithography [24], [25].

Here, we test the chip-scale PVD system by depositing Pb. The thermal evaporator was measured to produce a flux of $7.2\,\mathrm{\AA\,s^{-1}}$ at a separation $\sim 1\,\mathrm{mm}$ from the mass sensor. To produce this flux, the thermal evaporator consumed ($176.7\,\mathrm{mW}$ of power and used a low voltage ($9.5\,\mathrm{V}$ DC). The evaporator also has a modest footprint ($0.25\,\mathrm{mm^2}$) which opens the possibility of putting many evaporators on the same substrate and evaporating multiple materials in parallel. This potential capability is particularly of interest for combinatorial material preparation for new material discovery [26].

MEMS based thermal evaporators have been demonstrated previously by Imboden et al. and Han et al. [21], [27]. They used a surface micro-machining process (PolyMUMPs by MEMSCAP, inc.) to produce floating silicon plates suspended by two compliant springs [28]. The plates were heated by running a current through the springs. Materials were deposited onto the plates using a traditional PVD system and then re-evaporated from the plates in a controlled manner. The thermal evaporator presented in this work is similar in design and function to the evaporators presented Imboden et al. and Han et al but are larger scale, thus addressing an application space unmet by these previous systems or traditional PVD systems. For clarity, throughout the rest of the work, we will refer to the evaporators presented by Imboden et al. and Han et al. as microscale evaporators and the new evaporator presented here as a mesoscale evaporator.

Like the microscale evaporator, the mesoscale evaporator consists of a floating plate supported by two compliant springs that also serve as heating elements. Differently, the mesoscale evaporator is made using a silicon-on-insulator (SOI) process (SOIMUMPs by MEMSCAP, inc.) [29]. Consequently, the heating elements and plate on the mesoscale evaporator are about ten times thicker than the microscale evaporators. Stemming from this difference, there are several trade-offs between the microscale and mesoscale evaporators.

The microscale evaporators have faster thermal time constants owing to their lower mass ($<10\,\mathrm{ms}$), and they have a
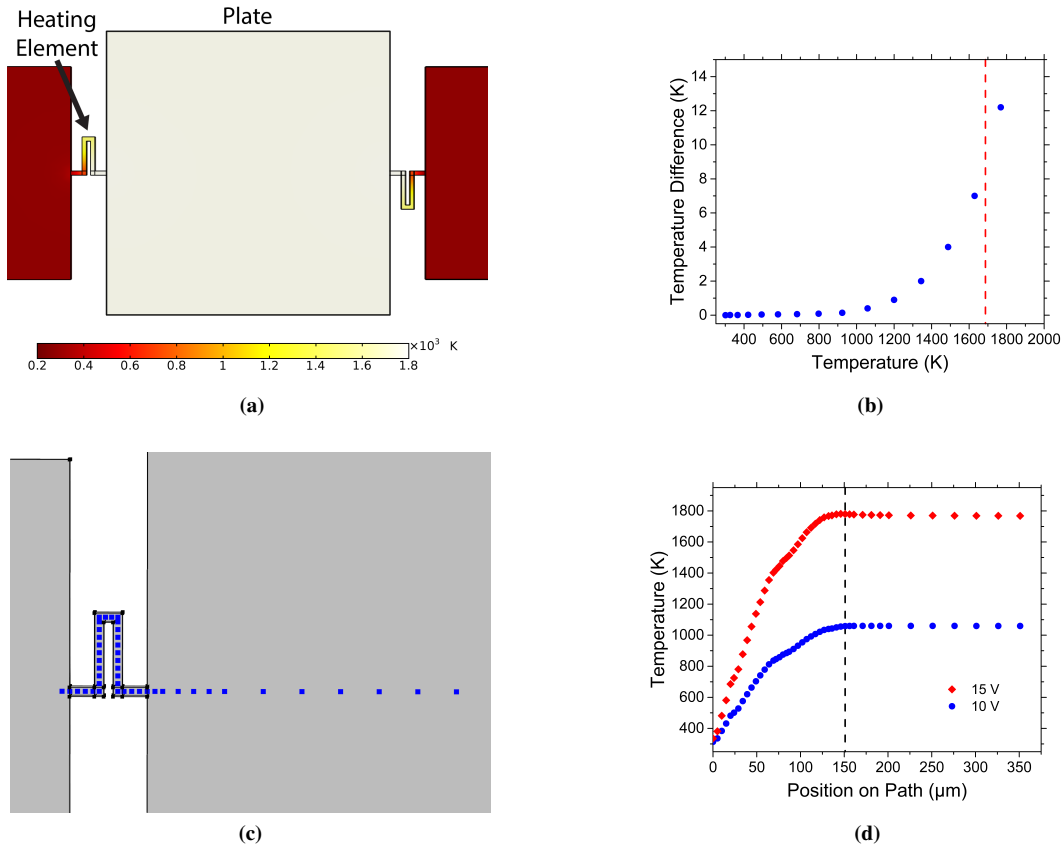
Fig. 1: Simulation data (Comsol Multiphysics) for the temperature profile of a mesoscale evaporator with $15\,\mathrm{V}$ and $10\,\mathrm{V}$ potential difference from one side to the other. At high temperatures, the profile remains relatively uniform because of the nature of blackbody radiation (a) Color plot of the surface temperature of the micro-source at $15\,\mathrm{V}$. (b) Plot of the difference between peak heater temperature and average plate temperature vs. the average plate temperature. The red line indicates the melting point of silicon. (c) Image of a heating element and part of plate with blue squares indicating the points plotted in (d). (d) Plot of the temperature at the points indicated in (c) vs. the position of the point along the path with the first point being at 0. The dotted line indicates the edge of the plate.

smaller footprint. Mesoscale evaporators can hold $> 100\times$ the material that has been demonstrated for microscale evaporators ($>12\,000\,000\,\mu\mathrm{m}^3$ vs. $\sim110\,000\,\mu\mathrm{m}^3$). Additionally, due to their increased mechanical rigidity, they can be loaded by mechanically placing material onto the plate with tweezers, a probe station or a pick-and-place system, obviating the need to use a traditional PVD system to load the plate.

When used at low temperatures ($<10\,\mathrm{K}$), microscale evaporators deposit quench condensed thin films that show no evidence of island growth. This is attributed to the adatoms having little or no mobility when they land on the target, and it is different than quench condensed films deposited with traditional PVD systems [14], [30]. This behavior opens up the possibility of using microscale evaporators as a material source in a FoC single atom lithography system. Currently, it remains an open question whether mesoscale evaporators can reproduce this unique behavior.

Microscale evaporators have also been used to deposit eight different materials (Al, Ag, Au, Cu, Fe, In, Pb and Sn) [27]. While mesoscale evaporators have only been demonstrated with Pb, we expect that mesoscale evaporators will work with

all of these materials, but it has not been demonstrated to date.

The mesoscale thermal evaporator is only half of the system. The other half is a mass sensor that can measure the the deposition rate in situ. Mass sensors have been extensively studied both using MEMS [31]–[36] and NEMS [37]–[40]. In addition to being used as film thickness monitors, mass-sensors are also can be used as chemical, biological, and gas sensors. Single atom resolution or better has been demonstrated using carbon nanotubes as resonators [37], [38]. Custom MEMS mass sensors have also been used as film thickness monitors in FoC systems [21], [27].

Here, we demonstrate that a mass sensor can be made from a commercial device (JTX210) [41]. Using a commercial device gives advantages both in terms of cost and ease of implementation. It may be the ideal solution for laboratory scale setups where an adequate mass sensor is needed quickly and reliably. The minimum Allan deviation was found to be $21.9\,\mu\mathrm{Hz}$ with $3\,\mathrm{s}$ time averaging. This corresponds to $2.65\,\mathrm{fg}$ and 7.79E-5 monolayers of Pb.

(a)

(b)

(c)

(d)

(e)
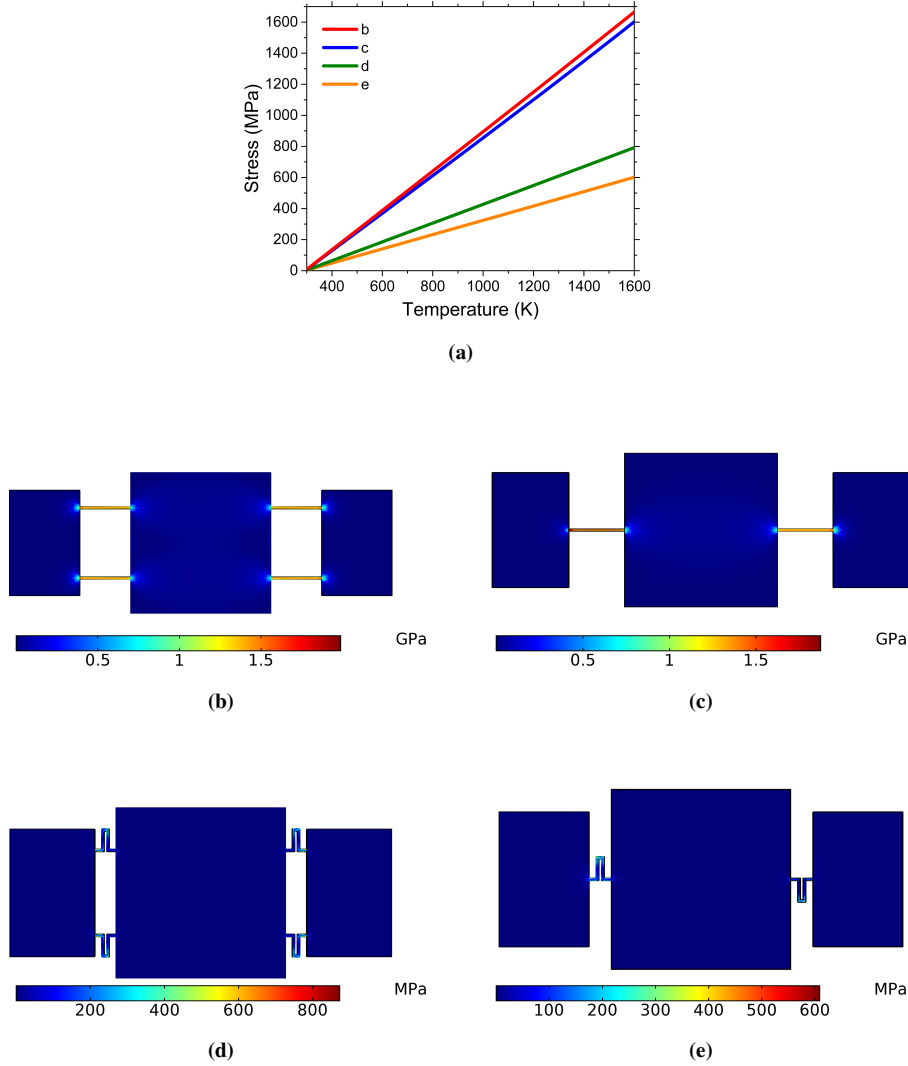
Fig. 2: Simulation data (Comsol Multiphysics) for various designs of heaters and plates (a) Graph of average plate surface temperature vs. maximum stress in the heater. The legend references (b-e). (b-e) Color plots of stress for various mesoscale evaporator designs at 15 V. In all cases, the plate is 400 μm×400 μm, and the line width of the heater is 6 μm.

II. DESIGN

The design of the mesoscale evaporator consists of a 400 μm×400 μm suspended plate connected to the substrate by two heating elements. The thickness for both heating elements and the plate is 25 μm set by the SOIMUMPs fabrication process. Heating element designs were tested using finite element analysis (FEA) in Comsol Mulitphysics.

The primary goal of the design is to reach the highest possible temperature before failure. Two failure modes were considered during the design process. First, the melting of the heating element was considered. The maximum possible temperature of the plate is the melting point of silicon. To approach this maximum temperature, the maximum temperature of the heating element cannot be significantly greater than the average temperature of the plate. Otherwise, the heating element will melt while the plate temperature is still low.

FEA of the difference between the plate and heating element temperature can be seen in Fig. 1. The temperature across the plate and from the plate to the heating element is uniform. The uniform behavior is expected at low temperatures where the only significant heat loss at the plate is conduction through the heating elements. At high temperatures, radiation must be considered. The nature of radiation cooling keeps the temperature uniform at high temperatures [21]. The power radiated by a unit of area is given by the Stefan-Boltzmann law:

$$P = \epsilon \sigma T^4 \tag{1}$$

where P is the power radiated per unit area, ϵ and σ are constants, and T is the temperature. The T^4 dependence means that any area whose temperature is higher will cool significantly more, minimizing the temperature differences. FEA estimates that the difference between the maximum temperature of the heating element and the average temperature of the plate is 0.4 K when the plate
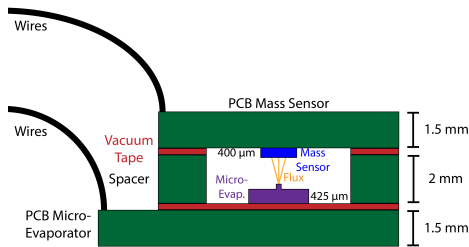
Fig. 3: Cross-section diagram of the setup for measuring the flux of the mesoscale evaporator. The setup operates in a vacuum chamber with pressure <200 mtorr. The thickness of the mass sensor package is $400\,\mu m$, but the thickness from the base to the top of the active element (the surface of the quartz oscillator) is only $320\,\mu m$. The distance from the top of the mesoscale evaporator plate is $1255\,\mu m$ and the distance from the top of the loaded metal at the start of evaporation is $955\,\mu m$.

is at $1059\,K$ and $12.2\,K$ when the plate is at $1769\,K$. For this device, differences above the melting point of silicon ($1687\,K$) are irrelevant to performance. However, it should be noted, when considering a design with higher temperature materials, that at sufficiently high temperatures significant differences between plate and heater temperature would be seen as discussed in [42].

The second failure mode considered was fracturing of the heating element due to stress from thermal expansion. Fig. 2 shows data from FEA of the stress in various heating element designs at different temperatures. Heating elements with bends to increase compliance were found to have less stress than straight lines because they can relieve stress from thermal expansion by deforming. Additionally, two heating elements were found to have less stress than four heating elements because they further constrain deformation that could relieve stress.

Consequently, the heating element designs in this work are compliant bends, and there are only two (one on either side). To decrease stress concentration further, curved structures and fillets were used to eliminate stress concentration at corners.

III. Setup

A simple setup was designed for measuring the performance of the PVD system. The setup is outlined in Fig. 3. The two primary elements are the mesoscale evaporator and mass sensor. Both sit on custom printed circuit boards (PCBs). The mesoscale evaporator is electrically connected to the PCB by gold ball bonds bonded to gold pads on the PCB. The mass sensor is soldered onto the PCB. The two PCBs are connected with double-sided vacuum tape and a spacer PCB that is a square ring with a small cut in a section to allow gas to escape during pump down. A hole was drilled in the mass sensor PCB next to the mass sensor to facilitate aligning the mass sensor and the mesoscale evaporator.

The distance between the top of the evaporator and the
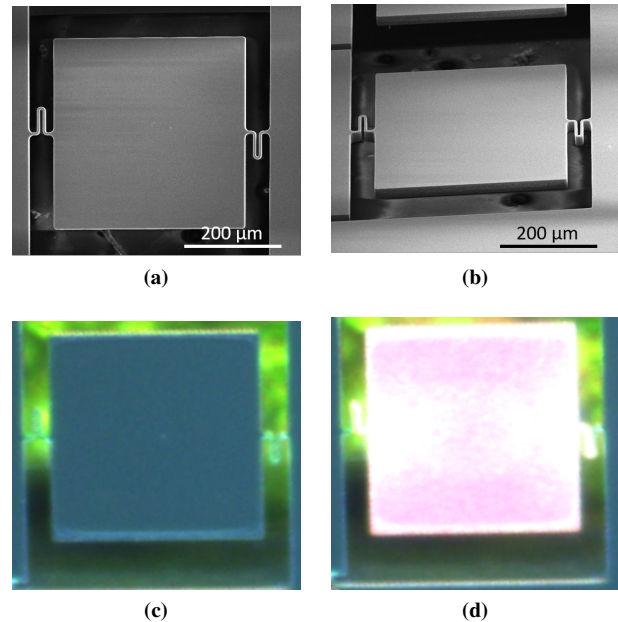
Fig. 4: Images of an unloaded mesoscale evaporator plate. (a,b) SEM images of the mesoscale evaporator plate. (c) Optical microscope image of the plate under vacuum with $0\,V$ DC applied. (d) Optical microscope image of the plate under vacuum with $10\,V$ applied. Black-body radiation from the heating is visible.

active surface of the mass sensor varies the evaporation rate. In this setup, the spacer is $2\,mm$ thick, and while the package of the mass sensor is $400\,\mu m$ thick, the distance from the bottom of the package to the top of the active surface is only $320\,\mu m$. The mesoscale evaporator chip is $425\,\mu m$ thick and the metal placed on top of it is $\sim310\,\mu m$. The separation between the top of the metal and the active surface of the mass sensor is $955\,\mu m$.

IV. Performance

A. Mesoscale Evaporator

Images of the mesoscale evaporators as they come from the foundry can be found in Fig. 4. Additionally shown are optical microscope images of the mesoscale evaporator being heated with $0\,V$ and $10\,V$ under vacuum. Black-body radiation can be seen in the $10\,V$ image. The current through the mesoscale evaporator was monitored with an oscilloscope while the plate was heated with various voltages. The current data contains information about the temperature of the heating elements because the resistance of the poly-silicon depends on temperature. Fig. 5a-b show steady state current and resistance vs. voltage. As can be inferred from Fig. 5b, the resistance initially rises with temperature and then begins to decrease. This is due to transitioning from the extrinsic to intrinsic regimes of the doped poly-silicon. In the extrinsic regime, carrier concentration is constant with temperature because it is determined by the doping level. Resistance increases with temperature in the extrinsic regime because of the decreasing

mobility of the carriers. As the temperature continues to increase, eventually part of the heating elements move into the intrinsic regime where carrier concentration increases with temperature. The effect of the new carriers is greater than the decreasing mobility, and resistance goes down with temperature [43].

The temperature dependence of the resistance allows us to probe thermal characteristics of the mesoscale evaporator. Fig. 5c shows a normalized current vs. time for several different voltages. The time it takes the current to reach steady state depends on the thermal time constant of the system. Fig. 5d shows the current vs time after $8.5\,\mathrm{V}$ is applied to the mesoscale evaporator. The data is fit with an exponential decay

$$I = c_1 e^{\frac{-(t-c_2)}{\tau}} + c_3 \qquad (2)$$

where I is the current, c_1 is a scaling constant, c_2 and c_3 are translation constants, t is time after the pulse was applied, and τ is the thermal time constant. For $8.5\,\mathrm{V}$, the thermal time constant was found to be $\sim 38\,\mathrm{ms}$. The same fit has been applied to data for voltages from $2\text{-}8\,\mathrm{V}$. Thermal time constants range from $34\text{-}48\,\mathrm{ms}$. It takes ~ 4.6 thermal time constants to reach 99% of the final temperature. Consequently, heating the mesoscale evaporator plate takes $156\text{-}221\,\mathrm{ms}$. This is only for a bare plate, as adding material to be evaporated slows this further.

One of the primary advantages of the mesoscale evaporators in this work over previous works is the loading process. The mesoscale evaporator can be mechanically loaded with $>0.01\,\mathrm{mm}^3$. Fig. 6a shows a mesoscale evaporator with a piece of Pb on it. The Pb was cut from a 0.01 in. Pb wire with a razor blade and placed on the mesoscale evaporator. The Pb can be placed on the mesoscale evaporator either using a probe station, a probe tip held by hand, or tweezers. Once on the mesoscale evaporator plate, the Pb was melted onto the plate using the heating elements under vacuum as seen in Fig. 6b-c, also seen in Supplemental Movie 1 (SM1). This simple configuration is not stable over large depositions. As seen in Fig. 6d, after a long deposition large deposits of material build up on the heating elements. These deposits change the thermal properties of the heaters and more and more power has to be used to get the same flux rates.

A simple method of preventing deposition on the heating elements is to block the flux with silicon walls. As seen in Fig. 7 and Supplemental Movie 2 (SM2), the Pb can be placed inside four connected silicon walls and melted onto the mesoscale evaporator. Additional material can be added into the hole, if desired, until the hole is filled. All of the material can be depleted from the source without significant deposition onto the heating elements. The connected silicon walls were made by thinning a $600\,\mathrm{\mu m}$ silicon wafer using repeated dicing saw cuts down to a thickness of $310\,\mathrm{\mu m}$ (after each cut the blade was stepped by the blade distance in the horizontal direction), then deep reactive ion etching (DRIE) $200\,\mathrm{\mu m}$ square holes through the wafer, and finally, cutting the hole out of the wafer using a dicing saw to leave behind four $50\text{-}100\,\mathrm{\mu m}$ thick connected silicon walls. During the final dicing, the saw did not cut all the way through the material, but a thin layer of silicon was left at the bottom to prevent the
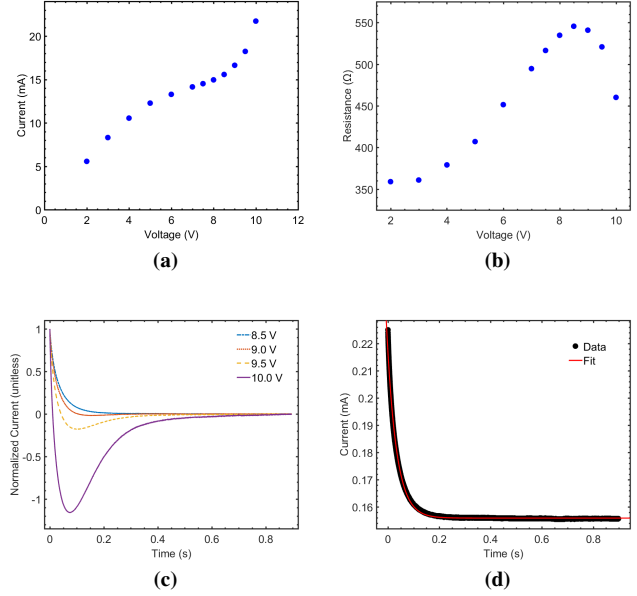
Fig. 5: Heating data of a bare mesoscale evaporator plate. (a) Current vs. voltage for the plate at steady state. (b) Resistance vs. voltage of the plate at steady state. This is the same data as (a). Resistance increases with temperature in the extrinsic regime and decreases with temperature in the intrinsic regime. (c) Current vs time after applying a voltage. Currents have been scaled and translated to have the same initial and final points. (d) Current vs time for the plate heating after having $8.5\,\mathrm{V}$ applied. The thermal time constant of the fit is $\sim 38\,\mathrm{ms}$. The same fit has been applied for voltages from $2\text{-}8.5\,\mathrm{V}$. Thermal time constants range from $34\text{-}48\,\mathrm{ms}$.

walls from shifting during the cutting process. This remaining material was later mechanically removed using tweezers and probe station tips.

B. Mass Sensor

The mass sensor is a re-purposed JTX210 quartz crystal oscillator (Juach Quartz). The oscillator was soldered to a PCB and the top of the package was removed with a razor blade under an optical microscope. Images of the mass sensor can be seen in Fig. 8. To prevent metal from depositing on the electrical leads and shorting the oscillator, a piece of vacuum tape was added to partially shield the mass sensor. This ensures that metal will only deposit on the paddles as seen in Fig. 8b. As metal deposits on the paddles, it shifts the resonant frequency of the mass sensor. The resonant frequency of the mass sensor was monitored using a phase locked loop [44]. The loop used a band pass filter and a lock-in amplifier to reduce the signal noise and a pulse generator (DG645 from Stanford Research Systems) as a phase shifter. Using a pulse generator instead of an Op amp based phase shifter was found to reduce the noise by $\sim 100\times$, increasing the resolution. The frequency was monitored with a frequency counter. The mass sensor's sensitivity was found by measuring the resonant frequency before and after depositing $100\,\mathrm{nm}$ of Pb onto the

(a)   **(b)**

(c)   **(d)**
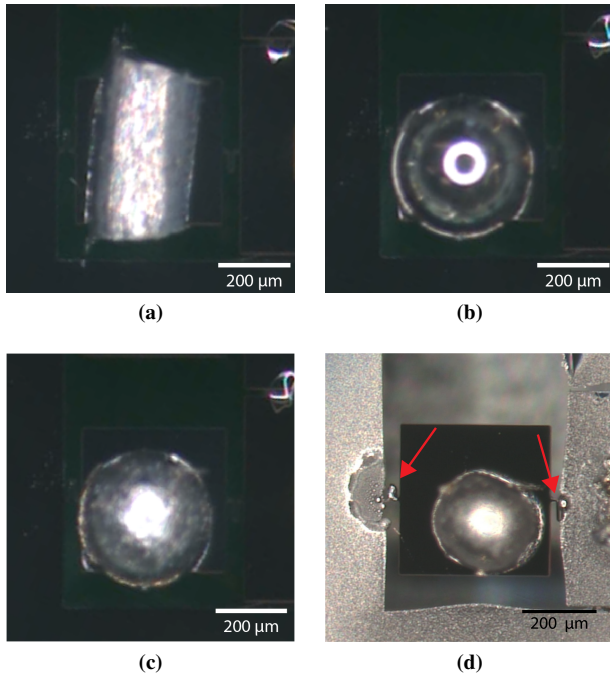
Fig. 6: Optical microscope images of loading a mesoscale evaporator. (a) Piece of Pb wire cut with razor blade is placed on mesoscale evaporator with tweezers. (b) Same piece of Pb melted by turning on the mesoscale evaporator (melts at $\sim$6 V). (c) Same piece of Pb solidified after turning off the mesoscale evaporator. (d) mesoscale evaporator after being used to deposit Pb. Indicated are the heating elements which have become covered in Pb, changing the thermal properties and lowering the temperature and flux at a given voltage. (a)-(c) also seen in SM1.

(a)   **(b)**

(c)

Fig. 7: Optical microscope images of loading a mesoscale evaporator with a silicon border to prevent deposition on the heating elements. (a) Border with cut piece of Pb that has been placed on the mesoscale evaporator plate using a probe needle. (b) The evaporator with the Pb melted using the mesoscale evaporator. (c) Solidified Pb inside the silicon border. Additional Pb can be added using a probe station. Also seen in SM2.

paddles using a conventional thermal evaporator. To fit into the conventional evaporator, the mass sensor had to be de-soldered from the PCB and then re-soldered after deposition. The sensitivity was measured to be $0.8745\,\mathrm{nm\,Hz^{-1}}$.

Fig. 8c shows the Allan deviation vs. averaging time for the mass sensor in a cryostat. A cryostat was chosen for this measurement because it had less mechanical noise than the setup used in the rest of this work. This was in an effort to find the minimum resolution of this type of mass sensor. The minimum Allan deviation was found to be $21.9\,\mathrm{\mu Hz}$ at 3 s time averaging. This corresponds to $2.65\,\mathrm{fg}$ and 7.79e-5 monolayers of Pb using the measured calibration and a monolayer thickness of $2.46\,\text{Å}$.

C. Evaporation

The mesoscale evaporator was used to deposit Pb onto the mass sensor. Fig. 9 shows data from four $25\,\mathrm{s}$ depositions with different voltages applied. Using the measured sensitivity of the mass sensor, at $9.5\,\mathrm{V}$, there was a deposition rate of $7.2\,\text{Å}\,\mathrm{s^{-1}}$. The steady state current at $9.5\,\mathrm{V}$ was $18.6\,\mathrm{mA}$ which corresponds to a power of $177\,\mathrm{mW}$. Because of the large amount of extra mass added to the system by the walls and the Pb, the thermal time constant increased. Fig. 10 shows

the first $2.5\,\mathrm{s}$ of data from the $8.5\,\mathrm{V}$ evaporation seen in Fig. 9a. The data has been fit with equation 2. The thermal time constant was found to be $317\,\mathrm{ms}$ which means it takes $\sim$1.46 s to turn on (reach 99% of the final temperature) the mesoscale evaporator.

V. CONCLUSION

Here, we present a novel MEMS-based PVD system. It consists of two devices: a mesoscale thermal evaporator and a mass sensor used as a film thickness monitor. The mesoscale thermal evaporator is made by fabless manufacturing using a multi-user commercial process. As produced by the foundry the devices are functional, but become unstable due to deposition on the heating elements. Placing four silicon walls on the plate shields the heating elements and stabilizes the deposition. The evaporator turns on in $\sim$1.5 s and reaches deposition rates of Pb as high as $7.2\,\text{Å}\,\mathrm{s^{-1}}$ from $\sim$1 mm away. At those deposition rates, the system used only $9.5\,\mathrm{V}$ and $177\,\mathrm{mW}$. It has only been demonstrated with Pb, but similar designs have been demonstrated with eight different materials (Al, Ag, Au, Cu, Fe, In, Pb and Sn) [27]. It is believed that these materials could be deposited with the evaporator presented here as well.

The mass sensor is a re-purposed JTX210 quartz crystal oscillator (Juach Quartz). The top is removed to allow flux to be deposited onto the oscillator. The resonant frequency

(a)

(b)

(c)
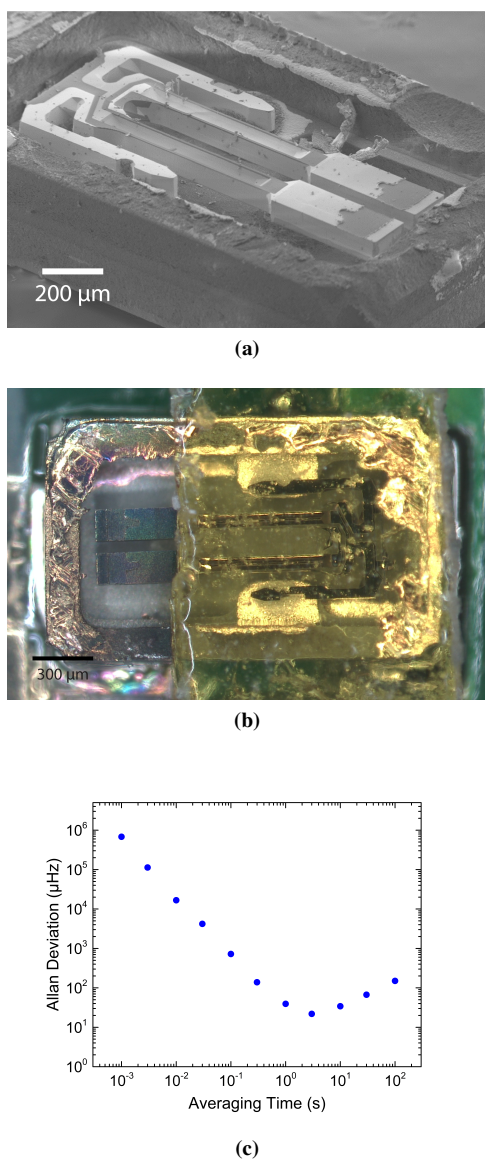
Fig. 8: Images of oscillator used as a mass sensor (JTX210, Jauch Quartz). (a) SEM image of oscillator. (b) Optical microscope image of resonator after evaporation of Pb. Vacuum tape was used to prevent deposition onto the exposed electronics. (c) Plot of Allan deviation vs. averaging time for the mass sensor in a cryostat. The minimum Allan deviation was found to be $21.9\,\mu$Hz at 3 second time averaging. This corresponds to $2.65\,$fg and 7.79E-5 monolayers of Pb.

is monitored using a phase locked loop. The phase shifter used here is an externally triggered pulse generator (DG645 from Stanford Research Systems) which was found to have $\sim 100\times$ less noise than phased locked loops that used op-amp based phase shifters. The sensitivity to Pb deposition was measured to be $0.8745\,$nm$\,$Hz^{-1}. The resolution was found to be $21.9\,\mu$Hz at $3\,$s time averaging. This corresponds to $2.65\,$fg and 7.79e-5 monolayers of Pb.

The PVD system presented here was designed to be part of a fab-on-a-chip, but it does have other potential applications. For example, it could be used as an inexpensive alternative

(a)

(b)
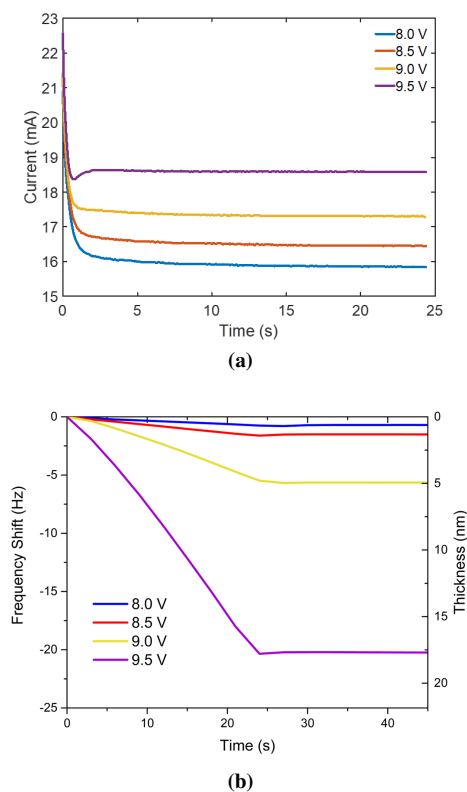
Fig. 9: Data from four depositions using the mesoscale evaporator loaded with Pb and with the Pb surrounded by four silicon walls to protect the heating element. (a) Current vs. time data for each deposition. (b) Frequency vs. time data for each deposition. Because the resonator sensitivity is $0.8745\,$nm$\,$Hz^{-1}, at $9.5\,$V, there was a deposition rate of $\sim 7.2\,$Å$\,$s^{-1}.

(a)
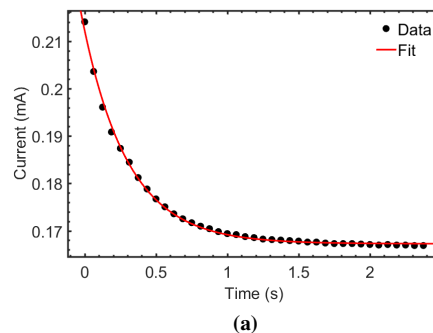
Fig. 10: A plot of the first $2.5\,$s of data from the $8.5\,$V evaporation shown in Fig. 9a. The data has been fit with equation 2. The thermal time constant was found to be $317\,$ms which means the mesoscale evaporator took $1.46\,$s to reach 99% of the final temperature.

to traditional PVD systems in certain research laboratories. It also can be used in heat sensitive environments (e.g. a cryostat) or with heat sensitive targets (e.g. biological films) because of its low power output. The low power output also would reduce error due to thermal drift in dynamic stencil lithography applications. Furthermore, the PVD system takes up $\sim 1\,\mathrm{cm}^3$ which allows it to be easily incorporated into existing systems to increase functionality. The size and speed also makes it potentially interesting for applications that require many different depositions (e.g. combinatorial material searches).

Acknowledgment

References

[1] D. M. Mattox, *Handbook of Physical Vapor Deposition (PVD) Processing*. Elsevier Inc., 2010.

[2] K. Habig, "Chemical vapor deposition and physical vapor deposition coatings: Properties, tribological behavior, and applications," *Journal of Vacuum Science & Technology A: Vacuum, Surfaces, and Films*, vol. 4, pp. 2832–2843, 11 1986.

[3] M. Ohring, *Materials Science of Thin Films*. London: Academic Press, 2nd ed., 2002.

[4] J. Singh and D. E. Wolfe, "Nano and macro-structured component fabrication by electron beam-physical vapor deposition (EB-PVD)," 1 2005.

[5] S. Govindarajan, J. J. Moore, J. Disam, and C. Suryanarayana, "Development of a Diffusion Barrier Layer for Silicon and Carbon in Molybdenum - A Physical Vapor Deposition Approach," *Metallurgical and Materials Transactions A: Physical Metallurgy and Materials Science*, vol. 30, no. 3, pp. 799–806, 1999.

[6] W. D. Westwood, "Physical Vapor Deposition," in *Microelectronic Materials and Processes*, pp. 133–201, Dordrecht: Springer Netherlands, 1989.

[7] V. Khanna, "Integrated Nanoelectronics," *Springer*.

[8] A. H. Eltoukhy, "A review of thin film media for magnetic recording," *Journal of Vacuum Science & Technology A: Vacuum, Surfaces, and Films*, vol. 4, pp. 539–542, 5 1986.

[9] P. Borisov, A. Hochstrat, V. V. Shvartsman, W. Kleemann, T. Eimüller, and A. F. Rodríguez, "Thin Cr ¡sub¿2¡/sub¿ O ¡sub¿3¡/sub¿ Films for Magnetoelectric Data Storage Deposited by Reactive E-beam Evaporation," *Ferroelectrics*, vol. 370, pp. 147–152, 10 2008.

[10] R. V. Petrova, R. R. Vanfleet, D. Richardson, B. Yao, and K. R. Coffey, "Characterization of individual L10 FePt nanoparticles," in *IEEE Transactions on Magnetics*, vol. 41, pp. 3202–3204, 10 2005.

[11] T. Alam, B. Wang, R. Pulavarthy, M. A. Haque, C. Muratore, N. Glavin, A. K. Roy, and A. A. Voevodin, "Domain engineering of physical vapor deposited two-dimensional materials," *Applied Physics Letters*, vol. 105, p. 213110, 11 2014.

[12] J. A. Garlow, L. K. Barrett, L. Wu, K. Kisslinger, Y. Zhu, and J. F. Pulecio, "Large-Area Growth of Turbostratic Graphene on Ni(111) via Physical Vapor Deposition," *Scientific Reports*, vol. 6, p. 19804, 4 2016.

[13] R. C. Dynes, J. P. Garno, and J. M. Rowell, "Two-dimensional electrical conductivity in quench-condensed metal films," *Physical Review Letters*, vol. 40, pp. 479–482, 2 1978.

[14] K. L. Ekinci and J. M. Valles, "Morphology of quench condensed Pb films near the insulator to metal transition," *Physical Review Letters*, vol. 82, pp. 1518–1521, 2 1999.

[15] S. Poran, M. Molina-Ruiz, A. Gérardin, A. Frydman, and O. Bourgeois, "Specific heat measurement set-up for quench condensed thin superconducting films," *Review of Scientific Instruments*, vol. 85, p. 053903, 5 2014.

[16] D. Pérez-Morelo, A. Stange, R. W. Lally, L. K. Barrett, M. Imboden, D. K. Campbell, V. A. Aksyuk, and D. J. Bishop, "Searching for the Casimir Energy," 4 2020.

[17] J. Wang, H. Huang, S. V. Kesapragada, and D. Gall, "Growth of Y-shaped nanorods through physical vapor deposition," *Nano Letters*, vol. 5, pp. 2505–2508, 12 2005.

[18] M. Imboden, H. Han, J. Chang, F. Pardo, C. A. Bolle, E. Lowell, and D. J. Bishop, "Atomic Calligraphy: The Direct Writing of Nanoscale Structures Using a Microelectromechanical System," *Nano Letters*, vol. 13, pp. 3379–3384, 7 2013.

[19] J. B. Reeves, R. K. Jayne, T. J. Stark, L. K. Barrett, A. E. White, and D. J. Bishop, "Tunable Infrared Metasurface on a Soft Polymer Scaffold," *Nano Letters*, 2018.

[20] J. B. Reeves, R. K. Jayne, L. Barrett, A. E. White, and D. J. Bishop, "Fabrication of multi-material 3D structures by the integration of direct laser writing and MEMS stencil patterning," *Nanoscale*, vol. 11, pp. 3261–3267, 2 2019.

[21] M. Imboden, H. Han, T. Stark, E. Lowell, J. Chang, F. Pardo, C. Bolle, P. G. del Corro, and D. J. Bishop, "Building a Fab on a Chip," *Nanoscale*, vol. 6, pp. 5049–5062, 4 2014.

[22] J. C. Eloy and E. Mounier, "Status of the MEMS industry," in *Proc.SPIE*, vol. 5717, 1 2005.

[23] B. Choubey, "Going Fabless with MEMS," *Sensors & Transducers Journal*, vol. 127, pp. 1–14, 2011.

[24] H. Guo, D. Martrou, T. Zambelli, E. Dujardin, and Gauthier, "Development of UHV dynamic nanostencil for surface patterning," in *Review of Scientific Instruments*, vol. 79, p. 103904, American Institute of PhysicsAIP, 10 2008.

[25] W. Steurer, L. Gross, R. R. Schlittler, and G. Meyer, "A variable-temperature nanostencil compatible with a low-temperature scanning tunneling microscope/atomic force microscope," *Review of Scientific Instruments*, vol. 85, p. 023706, 2 2014.

[26] Y. K. Yoo and X.-D. Xiang, "Combinatorial material preparation," tech. rep., 2002.

[27] H. Han, M. Imboden, T. Stark, P. G. del Corro, F. Pardo, C. A. Bolle, R. W. Lally, and D. J. Bishop, "Programmable solid state atom sources for nanofabrication," *Nanoscale*, vol. 7, pp. 10735–10744, 6 2015.

[28] A. Cowen, B. Hardy, R. Mahadevan, and S. Wilcenski, "PolyMUMPs Design Handbook a MUMPs® process,"

[29] A. Cowen, G. Hames, D. Monk, S. Wilcenski, and B. Hardy, "SOI-MUMPs Design Handbook a MUMPs® process,"

[30] M. Imboden, H. Han, T. Stark, and D. Bishop, "Cryogenic Fab-on-a-Chip Sticks the Landing," *ACS Nano*, vol. 11, pp. 8707–8716, 9 2017.

[31] H. Zhang and E. S. Kim, "Micromachined acoustic resonant mass sensor," *Journal of Microelectromechanical Systems*, vol. 14, pp. 699–706, 8 2005.

[32] W. Zhang, R. Baskaran, and K. L. Turner, "Effect of cubic nonlinearity on auto-parametrically amplified resonant MEMS mass sensor," *Sensors and Actuators, A: Physical*, vol. 102, pp. 139–150, 12 2002.

[33] T. P. Burg, A. R. Mirza, N. Milovic, C. H. Tsau, G. A. Popescu, J. S. Foster, and S. R. Manalis, "Vacuum-packaged suspended microchannel resonant mass sensor for biomolecular detection," *Journal of Microelectromechanical Systems*, vol. 15, pp. 1466–1476, 12 2006.

[34] W. Zhang and K. L. Turner, "Application of parametric resonance amplification in a single-crystal silicon micro-oscillator based mass sensor," *Sensors and Actuators, A: Physical*, vol. 122, pp. 23–30, 7 2005.

[35] H. S. Wasisto, S. Merzsch, A. Waag, E. Uhde, T. Salthammer, and E. Peiner, "Airborne engineered nanoparticle mass sensor based on a silicon resonant cantilever," *Sensors and Actuators, B: Chemical*, vol. 180, pp. 77–89, 4 2013.

[36] R. C. Lin, Y. C. Chen, W. T. Chang, C. C. Cheng, and K. S. Kao, "Highly sensitive mass sensor using film bulk acoustic resonator," *Sensors and Actuators, A: Physical*, vol. 147, pp. 425–429, 10 2008.

[37] K. Jensen, K. Kim, and A. Zettl, "An atomic-resolution nanomechanical mass sensor," *Nature Nanotechnology*, vol. 3, pp. 533–537, 9 2008.

[38] J. Chaste, A. Eichler, J. Moser, G. Ceballos, R. Rurali, and A. Bachtold, "A nanomechanical mass sensor with yoctogram resolution," *Nature Nanotechnology*, vol. 7, pp. 301–304, 4 2012.

[39] E. Forsen, G. Abadal, S. Ghatnekar-Nilsson, J. Teva, J. Verd, R. Sandberg, W. Svendsen, F. Perez-Murano, J. Esteve, E. Figueras, F. Campabadal, L. Montelius, N. Barniol, and A. Boisen, "Ultrasensitive mass sensor fully integrated with complementary metal-oxide-semiconductor circuitry," *Applied Physics Letters*, vol. 87, p. 043507, 7 2005.

[40] N. Kacem, J. Arcamone, F. Perez-Murano, and S. Hentz, "Dynamic range enhancement of nonlinear nanomechanical resonant cantilevers for highly sensitive NEMS gas/mass sensor applications," *Journal of Micromechanics and Microengineering*, vol. 20, p. 045023, 4 2010.

[41] "Quartz Crystal JTX210," tech. rep., 2017.

[42] M. Imboden, "High-Temperature Infrared Radiator Element And Methods," 2019.

[43] P. F. Weller, "An introduction to principles of the solid state. Extrinsic semiconductors," *Journal of Chemical Education*, vol. 48, p. 831, 12 1971.

[44] Guan-Chyun Hsieh and J. Hung, "Phase-locked loop techniques. A survey," *IEEE Transactions on Industrial Electronics*, vol. 43, pp. 609–615, 12 1996.